Ab Initio Investigation of Water Adsorption and Hydrogen Evolution on Co$_9$S$_8$ and Co$_3$S$_4$ Low-Index Surfaces

Marco Fronzi,*[,†,‡] M. Hussein N. Assadi,[§] and Michael J. Ford*[,‡]

[†]International Research Centre for Renewable Energy, State Key Laboratory of Multiphase Flow in Power Engineering, Xi'an Jiaotong University, Xi'an 710049, Shaanxi, China

[‡]School of Mathematical and Physical Sciences, University of Technology, P.O. Box 123, Broadway, Sydney, New South Wales 2007, Australia

[§]Center for Computational Sciences, University of Tsukuba, Tsukuba, Ibaraki 305-8577, Japan

ABSTRACT: We used density functional theory approach, with the inclusion of a semiempirical dispersion potential to take into account van der Waals interactions, to investigate the water adsorption and dissociation on cobalt sulfide Co$_9$S$_8$ and Co$_3$S$_4$(100) surfaces. We first determined the nanocrystal shape and selected representative surfaces to analyze. We then calculated water adsorption and dissociation energies, as well as hydrogen and oxygen adsorption energies, and we found that sulfur vacancies on Co$_9$S$_8$(100) surface enhance the catalytic activity toward water dissociation by raising the energy level of unhybridized Co 3d states closer to the Fermi level. Sulfur vacancies, however, do not have a significant impact on the energetics of Co$_3$S$_4$(100) surface.
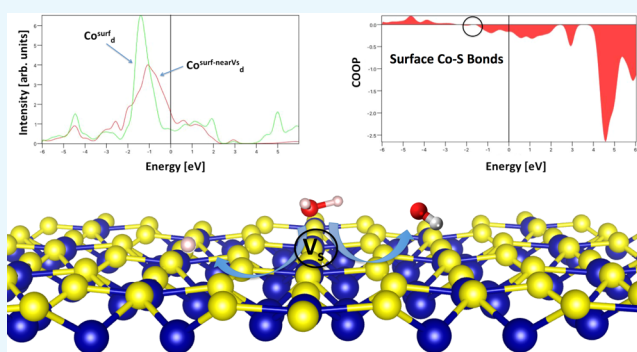
INTRODUCTION

Due to the depletion of carbon fossil fuel together with the environmental damage resulting from undesired emission from their combustion, finding new energy carriers is becoming a necessity.[1,2] Hydrogen represents a clean and renewable alternative energy carrier and can be used to replace to conventional and less environmental friendly fuels.

The production of molecular hydrogen can be obtained through water splitting that currently represents the most energetically favorable process, which however consists of only 4% of the total production due to the inefficiency of the present catalysts.[3−7] Another viable way is represented by thermal water splitting, where the necessary temperatures can be typically generated by either concentrating the sunlight or using waste heat from advanced nuclear reactors. However, this process suffers from a low efficiency due to the high temperatures, typically between 800 and 2500 K, necessary to obtain a complete reaction cycle.[8]

Recent analysis reports transition-metal sulfides (TM−S) that have interesting catalytic properties for several chemical processes, showing a pronounced selectivity, which is a fundamental property of a good catalyst. At the moment, the main technological application of TM−S concerns the process of hydrogen desulfurization. However, the primary step of the reaction shares hydrogen as a surface intermediate with the hydrogen evolution reaction (HER) and thus has a common elementary step, suggesting that the same catalyst should, in principle, perform well for both hydrogenation and hydrogen evolution reaction (HER).[9]

A particular class of interesting TM−S compounds are cobalt sulfides crystallized in pentlandite Co$_9$S$_8$ and linnaeite Co$_3$S$_4$ forms.[10,11] Recent studies show that Co$_9$S$_8$ and Co$_3$S$_4$ have catalytic activity and can be used in hydrogen and oxygen evolution reactions, where Co is a catalytic center.[12−15,17] These works also suggest that a specific micro and nano-structuring of cobalt sulfide may significantly increase its catalytic performance, as also known for CoS$_2$.[18] Pan et al. analyzed Co$_9$S$_8$ and Co$_3$S$_4$ for HER, and they experimentally observed that spherelike Co$_3$S$_4$ exhibits better electrocatalytic activity than the dandelion-like Co$_9$S$_8$ for HER.[15] Sidik et al. carried out theoretical investigations on (202) Co$_9$S$_8$ surface to analyze oxygen evolution reaction. They calculated the strength of the interaction between the surfaces and water, molecular oxygen, and hydroxyl radical, and they predicted non-negligible activity for water oxidation, suggesting a possible use of this crystal surface for water splitting.[12] However, although surface sulfur vacancies are often crucial in many catalytic processes and they may significantly affect the energetics for of many catalytic processes, their role in the catalytic activity of cobalt sulfides is not yet clear.[19,20]

The mentioned works suggest a potential use of Co$_9$S$_8$ and Co$_3$S$_4$ in water splitting; however, an investigation of thermal driven processes toward H$_2$ production has not been carried out yet. Therefore, a study of the energetics of water

adsorption and dissociation on stoichiometric and reduced cobalt sulfides, as well as hydrogen and oxygen adsorption, is crucial to understand the potential application of these crystals in technological applications. In particular, a detailed analysis of the adsorption energies of water and its fragments for a given surface is fundamental, since they provide excellent descriptors of the activation energy for water dissociation on that surface toward water splitting.[21]

Here, we present a comparative investigation of Co_9S_8 and Co_3S_4, with a focus on the role of sulfur vacancies in water dissociation and hydrogen evolution reaction. We apply density functional theory (DFT) calculations to analyze water, hydroxyl group, atomic oxygen, and atomic hydrogen adsorption energies in view of having a deeper understanding of the thermodynamics of the elementary processes that lead to HER. We compute electronic structure analysis and investigate the relation between stoichiometry of cobalt sulfides and catalytic properties for HER.

CALCULATION METHODS

The calculations presented in this work are performed by using a density functional theory approach, within the generalized gradient approximation (GGA) using the Perdew–Burke–Ernzerhof approach for the exchange–correlation term, and to describe correctly van der Waals interactions arising from the interaction of electric dipole moments, we include a correction as implemented in the method of Grimme.[22−24,29] We use periodic boundary conditions and a plane wave basis set as implemented in VASP code, wherein the core−valence interaction is described by projector augmented wave pseudopotential, with Co, O, S, and H valence electron in d^8s^1, s^2p^4, s^2p^4, and s^1 configuration, respectively.[25−28,30,31] The cutoff energy for the valence electrons has been set at 500 eV, and $(2 \times 2 \times 1)$ k-point mesh has been used. Slabs consist of (2×1), (1×1), and (1×1) expansion of the $Co_9S_8(110)$, (111), and (100) surfaces, respectively, and (1×1) expansion of the $Co_3S_4(100)$, (110) and (111) surfaces, with a thickness of 12−15 atomic layers, and a vacuum gap of ∼30 Å.[12,33] Full geometry optimization has been carried out for each system, and the convergence criteria for the energy and forces are 10^{-5} eV and 10^{-2} eV/Å, respectively. The energy barriers and transition states for water dissociation and hydrogen formation are located by using the climbing image nudged elastic band (NEB) method, which is an efficient method for searching the minimum energy path connecting the given initial and final states.[32] Although we report both pure GGA and GGA + vdW results for readers' reference, we develop our discussion on the basis of the GGA + vdW results as this functional encompasses more of the systems' physics.

RESULTS

Geometry and Energetics. Among cobalt sulfide compounds, the Co_9S_8 and Co_3S_4 structure materials crystallize in a pentlandite $Fm\bar{3}m$ structure and linnaeite $Fd\bar{3}m$, with lattice constants of 9.92 and 9.40 Å, respectively. Our calculated lattice constants and formation energies are 9.80 Å and −0.69 eV for Co_9S_8, and 9.29 Å and −0.75 eV for (Co_3S_4), in line with values reported in the literature.[34−36] In both structures, Co atoms occupy octahedral (Co^{oct}) and tetrahedral (Co^{tetr}) coordination, with a ratio of $Co^{oct}/Co^{tetr} = 1:8$ in Co_9S_8 and $Co^{oct}/Co^{tetr} = 2:1$ in Co_3S_4. Both crystals have Co−Co bonds with interatomic distances equal to or less than

those in Co metal. The calculated Co^{oct}−S and Co^{tetr}−S distances are 2.33 and 2.09−2.19 Å in Co_9S_8, whereas in Co_3S_4 Co^{tetr}−S, 2.00 Å and Co^{oct}−S, 2.31 Å.[34−36] Due to the symmetry of each surface, there is significant geometrical reconstruction of the three surfaces from the bulk cut, with a bond length change up to ∼0.1 Å, as reported in other works.[12] On the basis of crystallographic planes, many different surface compositions are possible for the pentlandite structure so we analyze a number of terminations for each orientation and report here the energetics of representative ones (see Table 1).

**Table 1. Surface Energies of the Co_9S_8 and Co_3S_4(100), (110), and (111) Surfaces**

Co_9S_8 hkl	surface energy (eV/Å²)
(100)	0.20
(110)	0.30
(111)	0.19
Co_3S_4 hkl	surface energy (eV/Å²)
(100)	0.13
(110)	0.16
(111)	0.32

We calculate the surface energy for each surface termination, which corresponds to the energy required to create a surface from the bulk structure, as follows

$$E_{surf} = \frac{1}{2A}\left[E_{slab} - \frac{M}{N}(E_{bulk})\right]$$

(1)

where A is the surface area, E_{slab} is the free energy of the slab used in the calculations, and E_{bulk} is the free energy of the bulk. M and N are the number of atoms in each slab and in the bulk, respectively.

By minimizing the total surface energy of a hypothetical particle of a given volume with respect to the energy of each calculated surface termination, we determine the nanoparticle geometry, as in the Wulff construction method, and show the predicted nanoparticles in Figure 1. The resulting particle
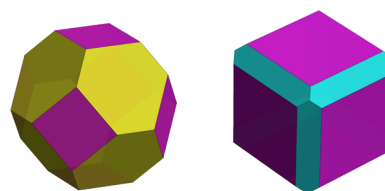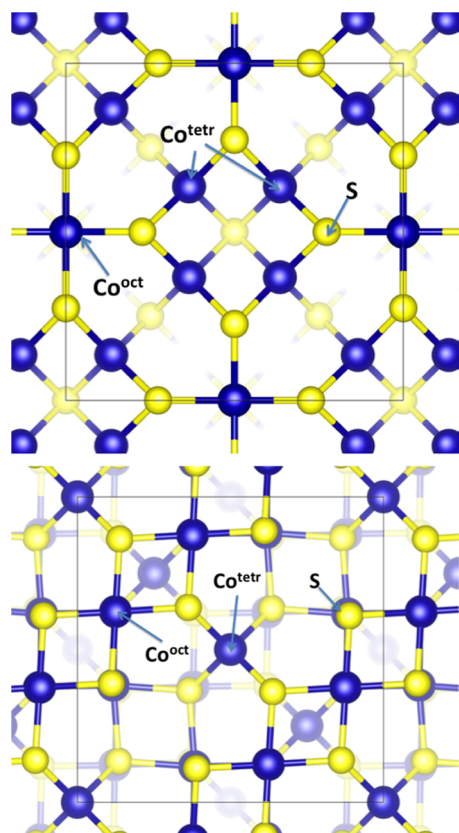

Figure 1. Schematic representation of the crystal shape obtained by Wulff construction, considering the surface energies reported in Table 1. Yellow, blue, and red facets indicate (111), (110), and (100) surface terminations, respectively.

shapes show that, in thermodynamic conditions, the surfaces exposed to the environment are (100) and (111) for Co_9S_8 and (100) and (110) for Co_3S_4. However, here, we focus our analysis of catalytic properties on the (100) surface, since it presents similar geometrical structure in both materials that enable us to highlight the intrinsic difference in the electronic structure and potential catalytic activity.

Both surfaces contain a mixture of Co and S sites; however, the main structural differences between Co_9S_8(100) and Co_3S_4(100) are the Co/S rate, which is 1:4 in Co_9S_8 and 1:2 in Co_3S_4(100), and that, although Co_3S_4 only exposes

Co^{oct}, Co_9S_8 exposes a mixture of Co^{oct} and Co^{tetr} with dominance of Co^{tetr}, as shown in Figure 2.

Figure 2. Schematic representation of $Co_9S_8(100)$ (top) and $Co_3S_4(100)$ (bottom) terminations. Here, blue and yellow spheres represent cobalt and sulfur atoms, respectively. The outermost layers of the cleaved surfaces contain both Co and S ions. In the picture, Co^{tetr} and Co^{oct} indicate Co ions in tetrahedral and octahedral coordination, respectively. Unit cell is delimited by a black line.

Adsorption Energies and Geometries. Although in realistic conditions water splitting and HER can present several intermediate phases, we are interested in analyzing the fundamental steps of the following total reaction

$$H_2O \rightarrow H_2 + \frac{1}{2}O_2 \qquad (2)$$

During thermal decomposition, the first step of eq 2 has been described in terms of water dissociation form adsorbed H ($H_2O \rightarrow H_{ad} + OH_{ad}$). Then, eventually, two adsorbed surface hydrogens next to each other react to form H_2 ($H_{ad} + H_{ad} \rightarrow H_2$).[37−39] The direct thermal splitting of water will require temperatures of ~2500 K, which makes its practical application very challenging. The fundamental limitation of the thermal splitting of liquid water is the fact that the ground state of oxygen is in a triplet spin configuration, whereas the ground state of water is in a singlet spin configuration. Therefore, breaking a water molecule requires a substantial quantity of energy to excite the molecule to a higher spin state before the dissociation. However, by exploiting the catalytic properties of some surfaces, water dissociation and molecular hydrogen formation can be achieved at temperatures below ~1300 K.[40]

In view of this, we can identify the required necessary characteristics of a good catalyst as follows: it must be able to

dissociate water and attract protons and at the same time still be able to desorb H_2. Experimentally, HER activity can be correlated to calculated hydrogen adsorption energies from density functional theory (DFT), where high activity corresponds to low Gibbs free energy of hydrogen adsorption (ΔG_H).[42,43] This is because a lower ΔG_H results in a strong binding of the atomic hydrogen and prevents desorption of H_2, whereas higher ΔG_H prevents the binding of atomic hydrogen on the catalyst surfaces. Accordingly, ΔG_H is considered as a good descriptor of HER activity and good catalysts are expected to have very small value of ΔG_H. On the other hand, to have an efficient reaction, water must be strongly adsorbed and easily split on the surface. Therefore, the total reaction should have a high water dissociation energy and at the same time, low hydrogen adsorption energy. We calculate the zero point energy upon adsorption to be ~0.4 eV H and ~0.1 eV for H_2O, OH, and O, calculated considering the vibrational frequencies of the species in gas phase and those of the outermost surface atomic layer. Although this contribution to the total energy is significant, it is very similar in the two systems and therefore it will not give considerable additional information to this comparative analysis. Also, we adopt the approach used by Muhich et al. They suggest using a "benchmark" material to predict the H_2 production capacities of given materials,[41] which is chosen as a standard against which to compare reduction enthalpies of candidate materials within a similar thermal water splitting class (i.e., a similar reaction mechanism). They assume that within a thermal water splitting reaction class, the reduction entropy of the benchmark materials is approximately the same. Therefore, when comparing the relative equilibrium extents of reduction between the two materials, the entropic terms cancel. According to these considerations, here, we approximate $\Delta G \cong \Delta E$.

We calculate adsorption energies values for H_2O, OH, O, and H adsorption energies, as follows

$$E_{ads} = \frac{1}{N}[E_{surf+mol} - (E_{surf} + E_{mol})] \qquad (3)$$

where $E_{surf+mol}$, E_{surf}, and E_{mol} are the energies of the molecule−surface system, the surface, and molecule in gas phase, respectively whereas N is the number of molecules adsorbed per supercell.

We obtain a minimum energy configuration for stoichiometric surfaces when water adsorbs on the top of Co atom in a flat configuration with the hydrogen atoms stretched toward sulfur sites, whereas OH adsorbs at Co site in a planar configuration, as schematically depicted in Figure 3. Atomic oxygen and hydrogen adsorb favorably at cobalt and sulfur sites, respectively. Upon vacancy formation, water adsorbs on the top of the vacancy with the hydrogen pointing upward, whereas hydroxyl group and atomic oxygen fill the vacancy, as depicted in Figure 4. Representative atomic distances upon adsorption on stoichiometric and reduced surfaces are listed in Table 4.

Now let us examine how V_S alters the adsorption energies on these two surfaces based on adsorption energies reported in Tables 2 and 3. We calculated the energy gain from a single water molecule dissociation, from the difference between OH−H adsorption, schematically represented in Figure 5, and the water molecule in gas phase. We obtain energy values of −1.02 and −0.98 eV on Co_9S_8 and Co_3S_4, respectively, indicating a very similar trend of the stoichiometric surfaces. On the other
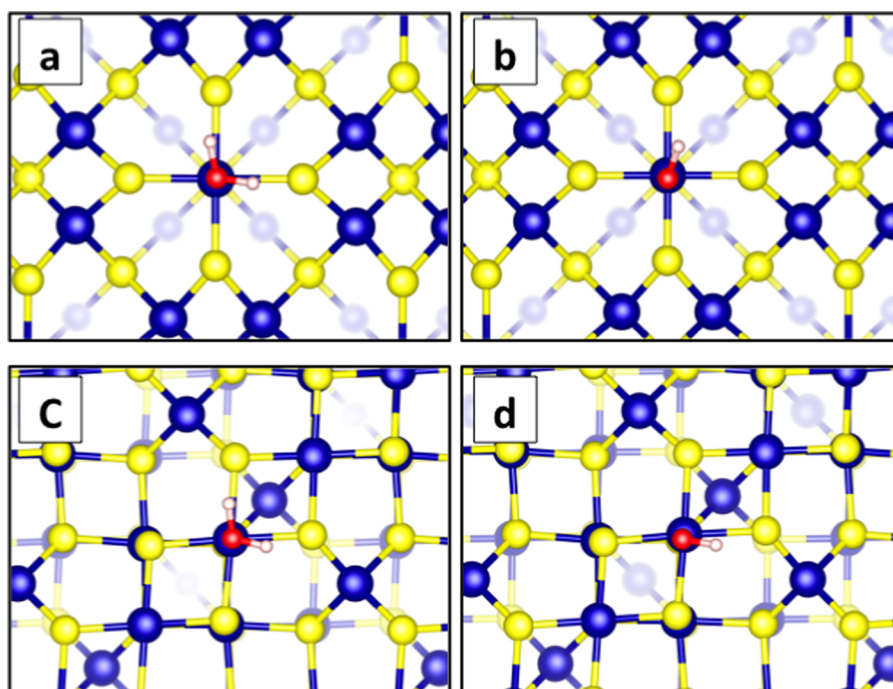
Figure 3. Schematic representation of water (a, c) and hydroxyl group (b, d) adsorption onto $Co_9S_8(100)$ (top) and $Co_3S_4(100)$ (bottom) surfaces. Here, blue, yellow, red, and white spheres represent, respectively, cobalt, sulfur, oxygen, and hydrogen atoms.
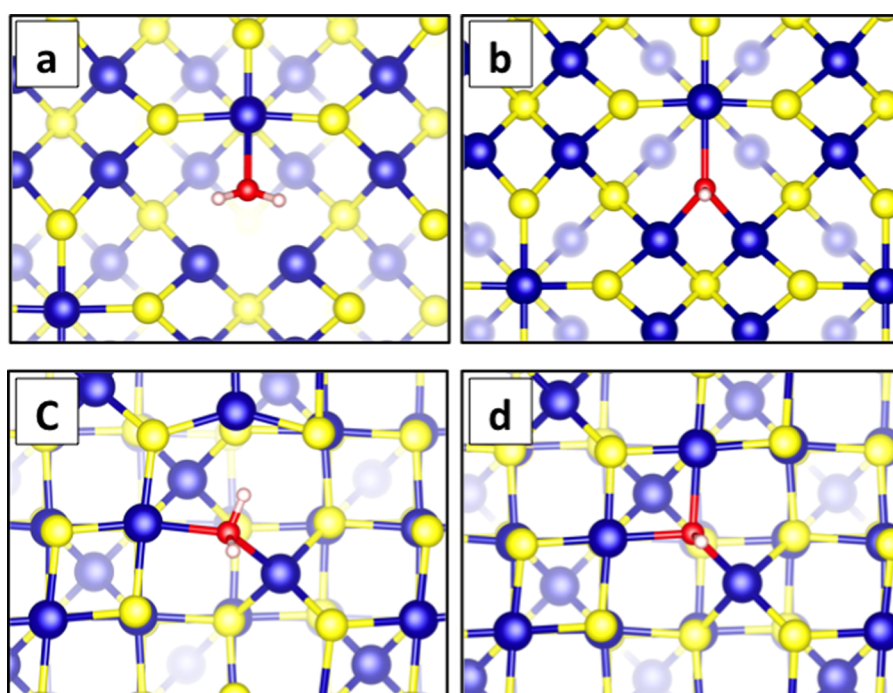
Figure 4. Schematic representation of water (a, c) and hydroxyl group (b, d) adsorption onto $Co_9S_8(100)$ (top) and $Co_3S_4(100)$ bottom surfaces upon sulfur vacancy formation. Here, blue, yellow, red, and white spheres represent, respectively, cobalt, sulfur, oxygen, and hydrogen atoms.

hand, when the same value is calculated for the reduced surfaces, we obtain an energy of −0.91 eV on Co_9S_8 and −0.20 eV on Co_3S_4, suggesting a significant difference of the energy trend of the reduced surfaces. The same conclusion can be reached also if we consider the energy balance of water dissociation reaction calculated from the separate H_2O, OH, and H adsorption energies, which gives an additional insight on the surface properties, since it takes into account the surface−adsorbate interaction strength of the individual

species. The energy gain from splitting one H_2O molecule is 2.71 eV for stoichiometric Co_9S_8 and 2.44 eV for stoichiometric Co_3S_4. Since these values are comparable to each other, the overall performance is then determined by the H absorption energy; the smaller it is, the better an H generator the surface is. Consequently, stoichiometric Co_3S_4 with H adsorption energy 0.23 eV smaller than that of Co_9S_8 is predicted to have superior HER performance. This prediction is indeed in agreement with previous calculations done by Pan

Table 2. H$_2$O, OH, O, and H Adsorption Energies Calculated for Stoichiometric and Reduced Co$_9$S$_8$(100) Surfaces^a

	ads. energy (eV)	
surface−adsorbate	GGA	vdW
(100)-H	−2.16	−2.22
(100)-O	−0.95	−1.08
(100)-OH	−2.04	−2.15
(100)-O−H	−1.24	−1.35
(100)-H$_2$O	−0.32	−0.52
(100)-OH−H	−0.99	−1.02
(100)-V$_S$−H	−2.92	−3.00
(100)-V$_S$−O	−2.78	−2.81
(100)-V$_S$−OH	−4.12	−4.24
(100)-V$_S$−OH	−3.32	−3.40
(100)-V$_S$−H$_2$O	−0.51	−0.80
(100)-V$_S$−OH−H	−0.80	−0.91

^{a}Energies are calculated with respect to the species in gas phase.

Table 3. H$_2$O, OH, O, and H Adsorption Energies Calculated for Stoichiometric and Reduced Co$_3$S$_4$(100) Surfaces^a

	ads. energy (eV)	
surface−adsorbate	GGA	vdW
(100)-H	−1.92	−1.99
(100)-O	−0.89	−0.95
(100)-OH	−2.18	−2.29
(100)-O−H	−0.70	−1.03
(100)-H$_2$O	−0.34	−0.50
(100)-OH−H	−0.96	−0.98
(100)-V$_S$−H	−1.68	−1.74
(100)-V$_S$-O	−2.07	−2.16
(100)-V$_S$−OH	−3.25	−3.34
(100)-V$_S$−O−H	−1.85	−1.90
(100)-V$_S$−H$_2$O	−0.38	−0.56
(100)-V$_S$−OH−H	−0.14	−0.20

^{a}Energies are calculated with respect to the species in gas phase.

et al.[15] The introduction of V$_S$, on the other hand, significantly increases the energy gain from water dissociation on Co$_9$S$_8$ surface compared to that on Co$_3$S$_4$ surface. In this case, the energy gain is 6.25 eV for Co$_9$S$_8$ and 4.94 eV for Co$_3$S$_4$. As a result, the energy gain upon water dissociation would be significantly higher on reduced Co$_9$S$_8$ surface. Nonetheless, one should note that introduction of V$_S$ also strengthens the adsorption hydrogen by lowering the H adsorption energy from −2.22 eV on stoichiometric Co$_9$S$_8$ surface to −3.00 eV on reduced Co$_9$S$_8$ surface. However, the energy gain in the first step of the reaction, that is water dissociations, would probably offset the enhanced H adsorption. As a result, we expect that the introduction of V$_S$ makes Co$_9$S$_8$ an efficient catalyst.

On the other hand, upon water dissociation, OH group is adsorbed favorably at V$_S$, filling the gap left from sulfur atom, with a strong adsorption energy of −4.24 and −3.34 eV, at the vacancy site. The high adsorption energies suggest a possible poisoning mechanism that will cancel the effect of the vacancy on the reaction energy balance. However, we calculated that hydrogen dissociation from OH will leave an oxygen atom trapped at the sulfur site with energies of −2.81 and −2.16 eV on the Co$_9$S$_8$ and Co$_3$S$_4$, respectively. As summarized in eq 2, we expect oxygen atoms to react to form molecular oxygen. Upon O$_2$ formation, we calculated a reduction of ∼1 eV when the trapped oxygen reacts to form O$_2$. Considering that this is a natural path of the total reaction under operating conditions, the energy values calculated for O$_2$ desorption from V$_S$ suggest
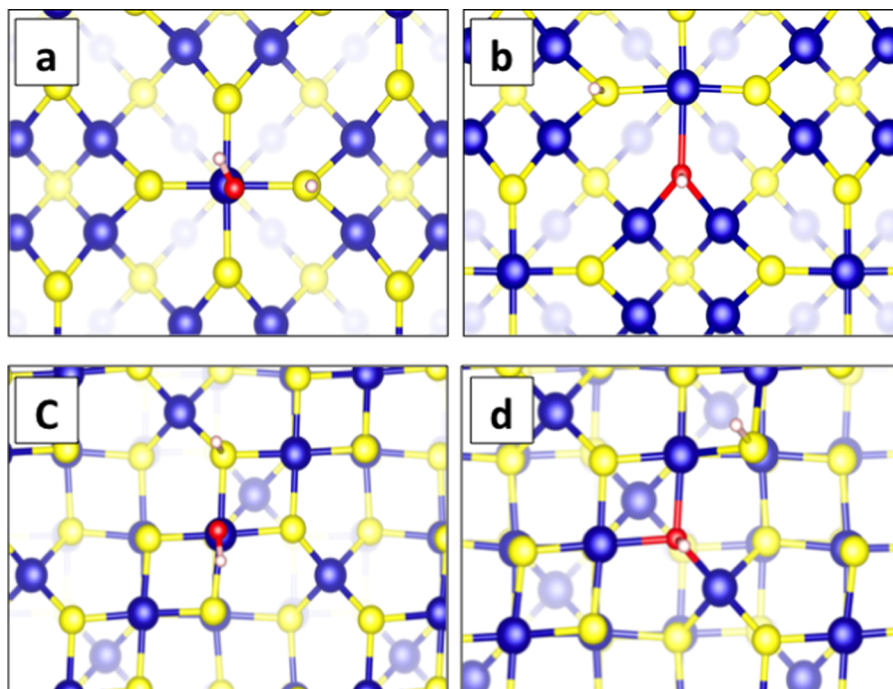
Figure 5. Schematic representation of hydrogen and hydroxyl group adsorption upon H$_2$O splitting, onto (a) stoichiometric and (b) reduced Co$_9$S$_8$(100) and (c) stoichiometric and (d) reduced Co$_3$S$_4$(100) surfaces. Here, blue, yellow, red, and white spheres represent respectively cobalt, sulfur, oxygen, and hydrogen atoms.
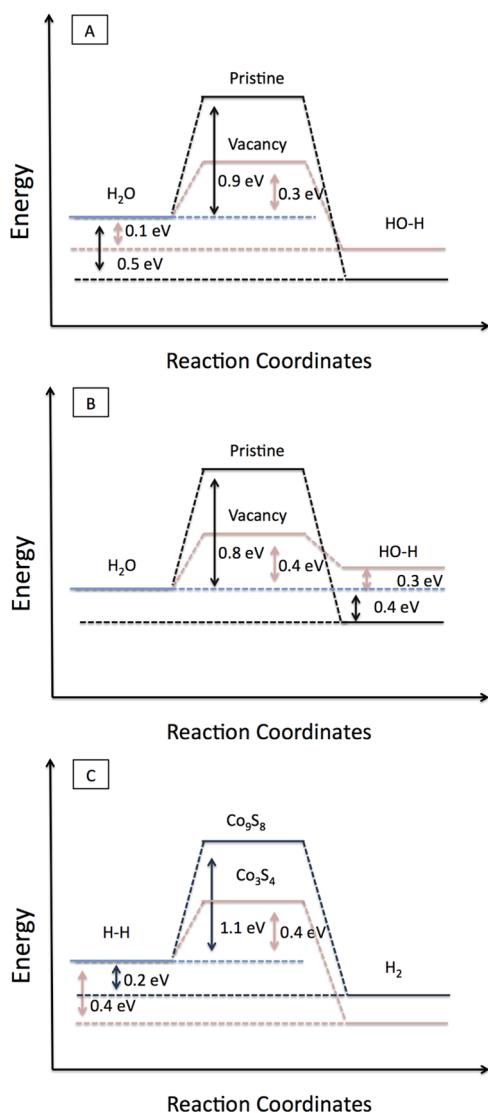
Figure 7. Calculated activation energies for H$_2$O dissociation into OH and H onto (a) pristine and defective Co$_9$S$_8$, (b) pristine and defective Co$_3$S$_4$, and (c) H$_2$ formation from H−H onto Co$_9$S$_8$ and Co$_3$S$_4$.

that the possible poisoning effect strongly depends on the operating temperature of the catalyst, which should ideally allow molecular oxygen desorption from the sulfur vacancy site.

To estimate the vacancy concentration and real stoichiometry of the surface in thermodynamic conditions, we calculated the vacancy formation energy as follows

$$E_{vac} = (E_{surf-vac} + E_{atom}) - E_{surf} \qquad (4)$$

If calculated with respect to the atomic sulfur atom, the cost to create a vacancy is Co$_9$S$_8$(100) is 5.07 eV and in Co$_3$S$_4$(100) is 4.43 eV, whereas the same value calculated with respect to the sulfur S$_8$ drops to 2.65 eV in Co$_3$S$_4$ and 2.01 eV in Co$_3$S$_4$, suggesting that in sulfur-rich conditions at operating temperature, the concentration of vacancies is relatively low.

However, the chemical potential of sulfur, controlled through temperature and partial pressure during synthesis, determines the abundance of sulfur vacancy at the surface. To have an insight into the sulfur vacancy formation and stability, we use the energy values calculated using DFT within the ab
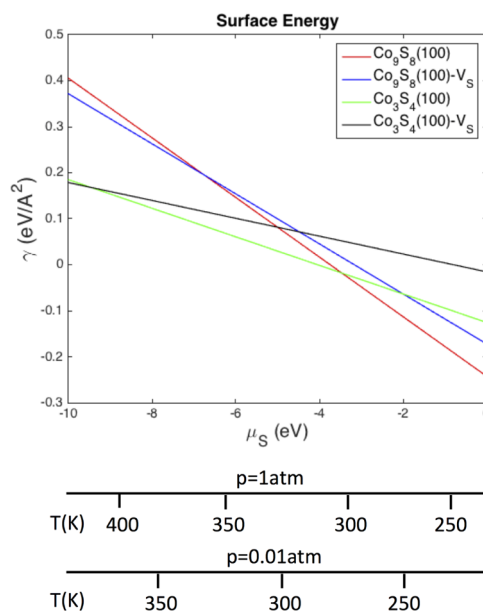
Figure 6. Calculated surface free energy of stoichiometric and reduced Co$_9$S$_8$(100) and Co$_3$S$_4$(100) surfaces as a function of the sulfur chemical potential μ_S. In the additional bars, the chemical potential of sulfur has been converted to temperature at two different partial pressures of the sulfur, 1 and 0.01 atm, respectively.

Table 4. Atomic Distances (in Å) upon Molecular and Atomic Adsorption on the Co$_9$S$_8$(100) and Co$_3$S$_4$(100) Surfaces[a]

surf.	H$_2$O−Co	OH−Co	O−Co	H−S
Co$_9$S$_8$	2.23	1.90	1.68	1.36
Co$_9$S$_8$−V$_S$	2.13	2.02	1.83	1.64
Co$_3$S$_4$	2.16	1.87	1.56	1.41
Co$_3$S$_4$−V$_S$	2.18	2.13	1.91	1.82

[a]For water and hydroxyl group, we report the distance from oxygen to surface cobalt atoms.

initio atomistic thermodynamics framework, as reported in the literature.[44,45] We calculate the surface energy as follows

$$\gamma(\{p_i\}, T) = \frac{1}{2A}\left[G - \sum_i N_i \mu_i(p_i, T)\right] \qquad (5)$$

where G is the surface energy of the slab with surface area A and the factor $\frac{1}{2}$ is due to the presence of two surfaces, one on each side of the slab. $\mu_i(p_i, T)$ is the pressure and temperature-dependent chemical potential of the various species i present in the system; in this case, i = Co and S. N_i is the total number of atoms in the component i of the system. Figure 6 shows the surface energies of reduced and stoichiometric Co$_9$S$_8$ and Co$_3$S$_4$. We find that for values of $\mu_S \leq -6.78$ and -9.64 eV, the reduced surfaces of Co$_9$S$_8$ and Co$_3$S$_4$ become stable if compared with the stoichiometric ones, suggesting a possible viable way to create conditions for the fabrication of reduced structures for both crystals. Using the definition of universal chemical potential for sulfur vapor formulated by Jackson et al., we converted, for a given partial pressure of sulfur in gas conditions, our energy values into temperature, and we found the transition between the stoichiometric and reduced surface to occur at ∼360 and ∼410 K at p = 1 atm, for Co$_9$S$_8$ and Co$_3$S$_4$, respectively, as shown in Figure 6.[46]
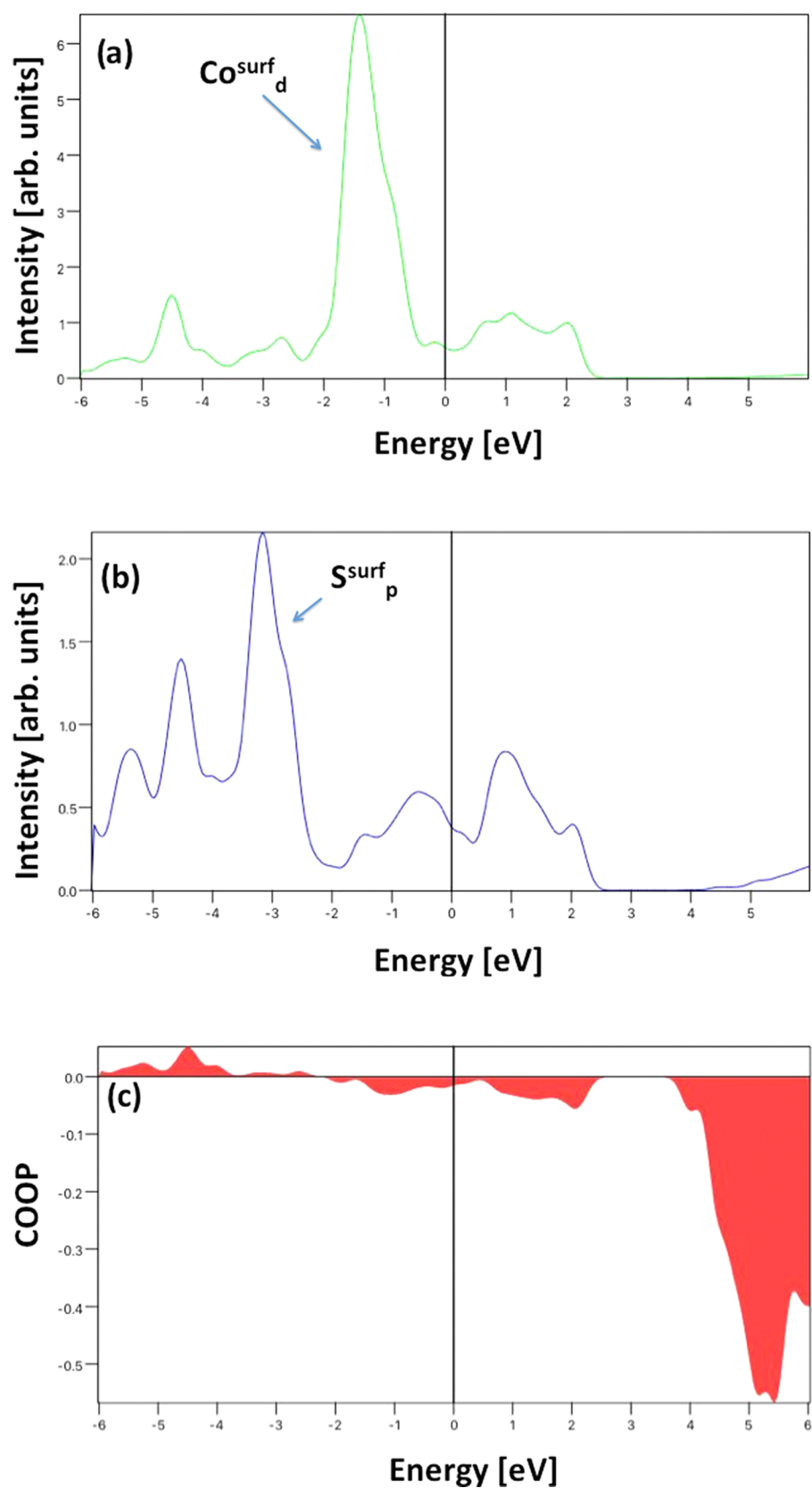
Figure 8. (a, b) pDOS of the $Co_9S_8(100)$ stoichiometric surfaces. (c) COOP analysis of the surface Co−S bond.

To have an insight into the reaction kinetics, we calculate the activation energies of water dissociation and molecular hydrogen formation by employing NEB method and schematically report the results in Figure 2. Interestingly, we found that the formation of molecular hydrogen is exothermic and that its activation energy is lower at $Co_3S_4(100)$ than at $Co_9S_8(100)$.[16] The energy reaction profile shows how both water splitting and hydrogen formation are exothermic reaction, with the exception of water dissociation onto
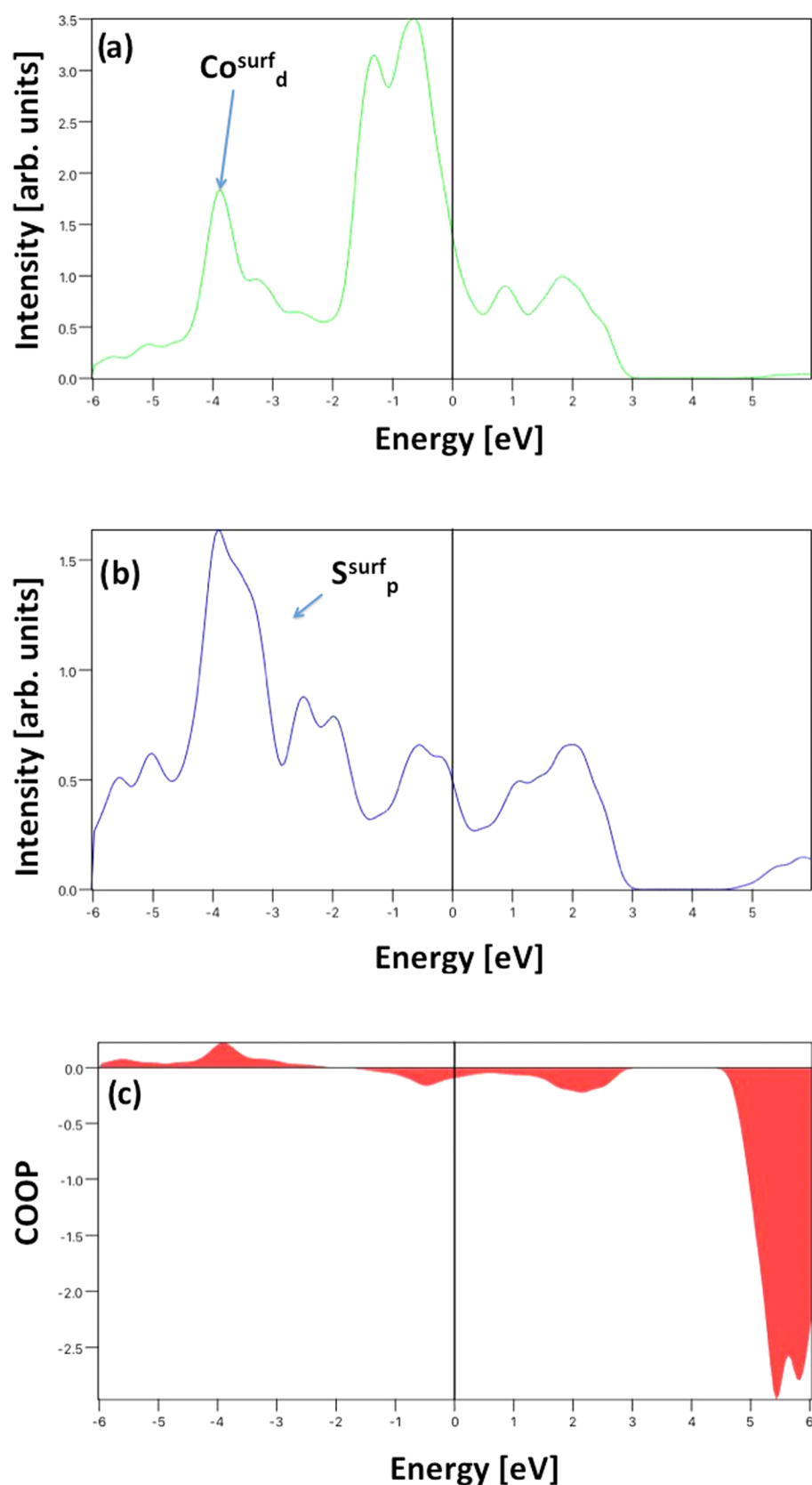
Figure 9. (a, b) pDOS of the $Co_3S_4(100)$ stoichiometric surfaces. (c) COOP analysis of the surface Co−S bond.

defective $Co_3S_4(100)$. However, since the total reaction indicated in eq 2 is endothermic, an intermediate step is supposed to be highly endothermic. We found one possible endothermic step to be OH dissociation, with an energy value of ∼0.80 eV in Co_9S_8 and ∼1.80

eV in Co_3S_4, as indicated by the energy values reported in Tables 2 and 3. Our results indicates that vacancy assists the reactions by decreasing the barriers in both crystals; however, hydrogen formation is kinetically favored on Co_3S_4 (Table 4).
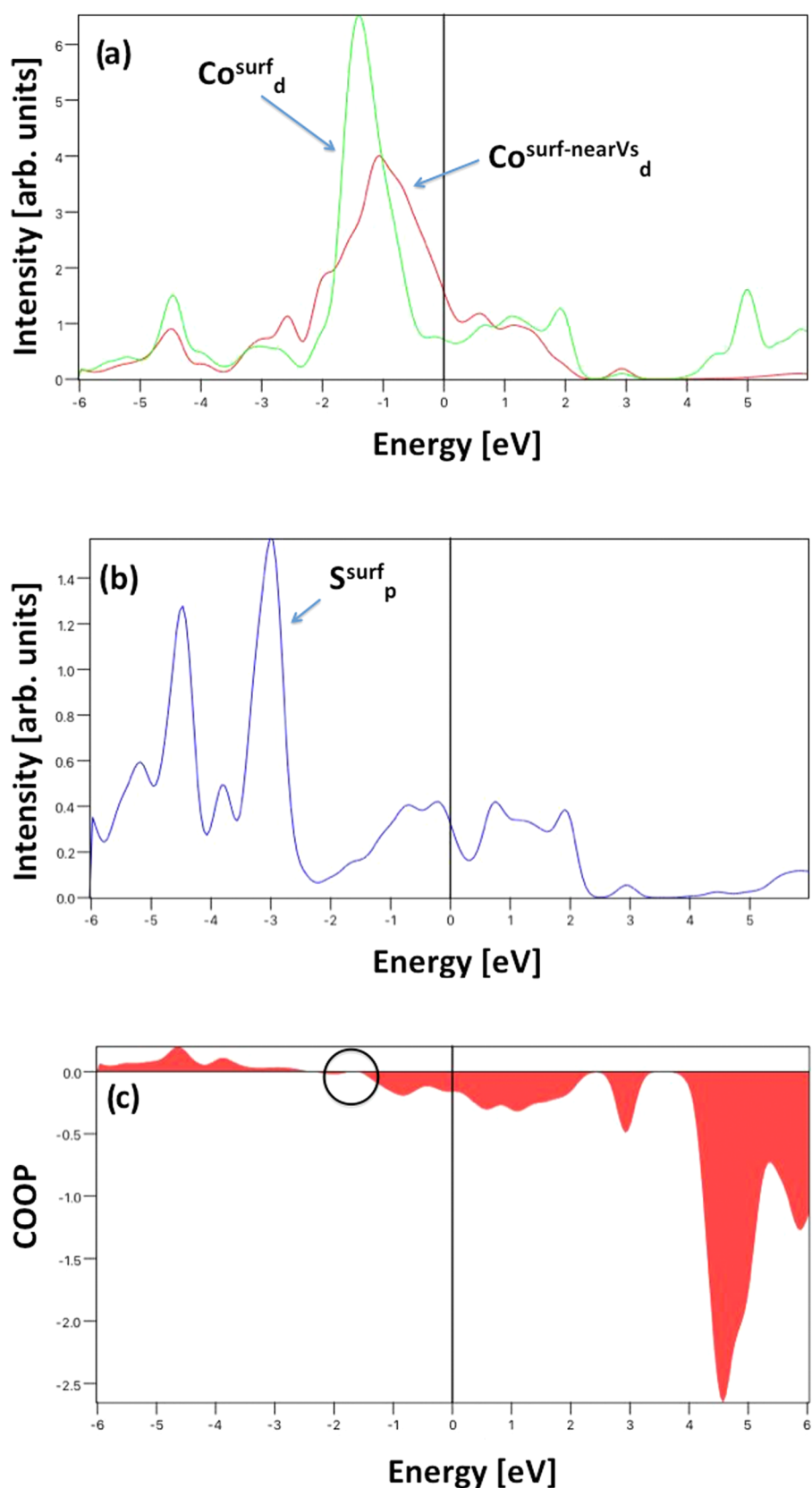
Figure 10. (a, b) pDOS of the $Co_9S_8(100)$ surfaces upon sulfur vacancy formation. In (a), low-coordinated cobalt located next to sulfur vacancy is indicated. (c) COOP analysis of the surface Co−S bond, with Co atom being low coordinated near sulfur vacancy.

Electronic Structure. Here, we report the analysis of the electronic structure of the two surfaces in their stoichiometric and reduced form (Figure 7). Figures 8 and 9 show the projected

density of states (pDOS) of surface cobalt and sulfur atoms in the stoichiometric slabs, together with the crystal orbital overlap population (COOP) analysis. Our electronic structure calculations
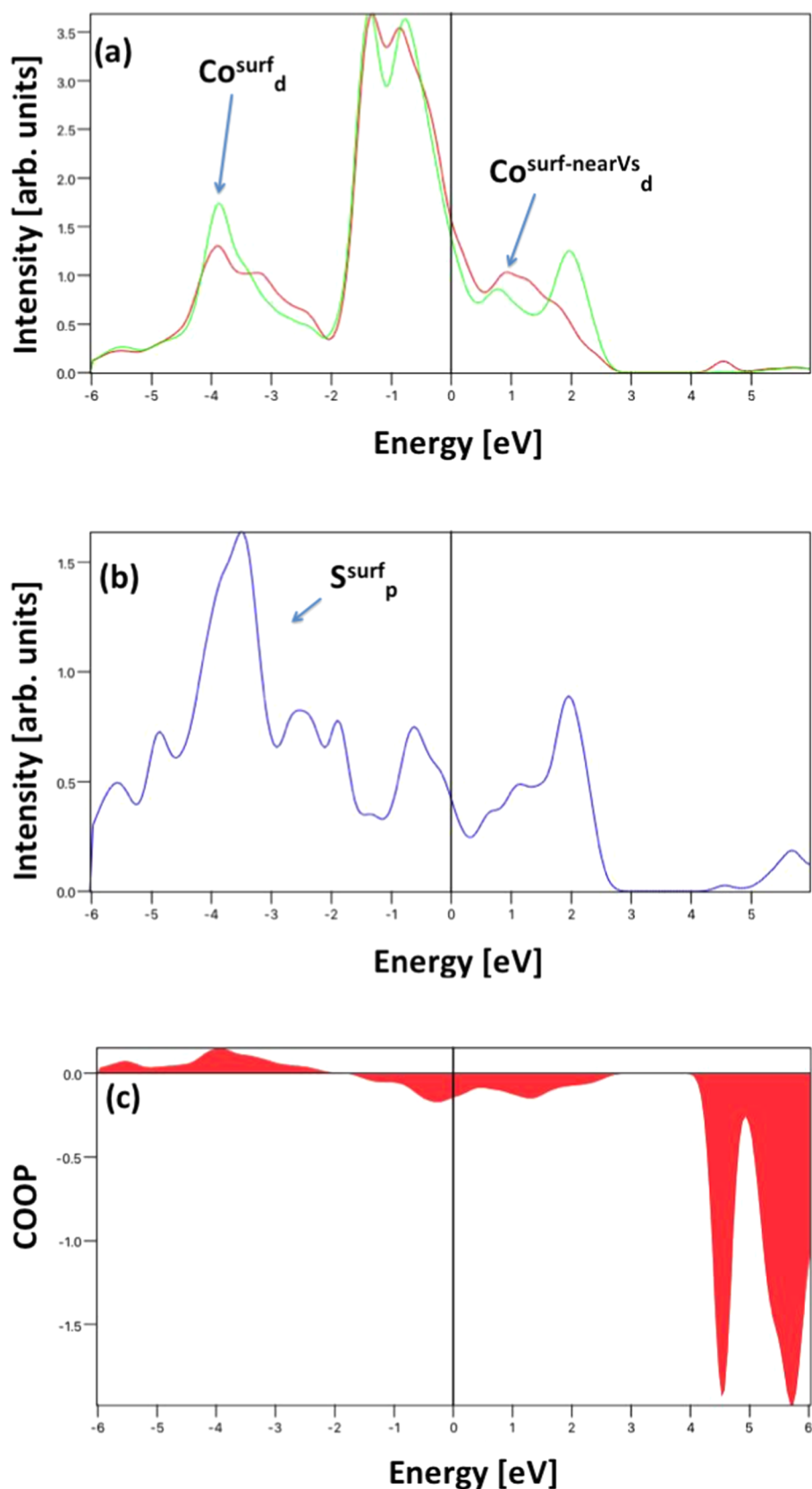
Figure 11. (a, b) pDOS of the $Co_3S_4(100)$ surfaces upon sulfur vacancy formation. In (a), low-coordinated cobalt located next to sulfur vacancy is indicated. (c) COOP analysis of the surface Co−S bond, with Co atom being low-coordinated near sulfur vacancy.

show that Co_9S_8 and Co_3S_4 have similar density of state function around the Fermi level, in line with the ability of the sulfide to conduct electronic currents. Both surfaces show a pronounced Co

3d peak right below the Fermi energy and an evident hybridization with the S 3p in a broad range. COOP analysis suggests the formation of bonding states below the Fermi energy at ∼−2 eV.
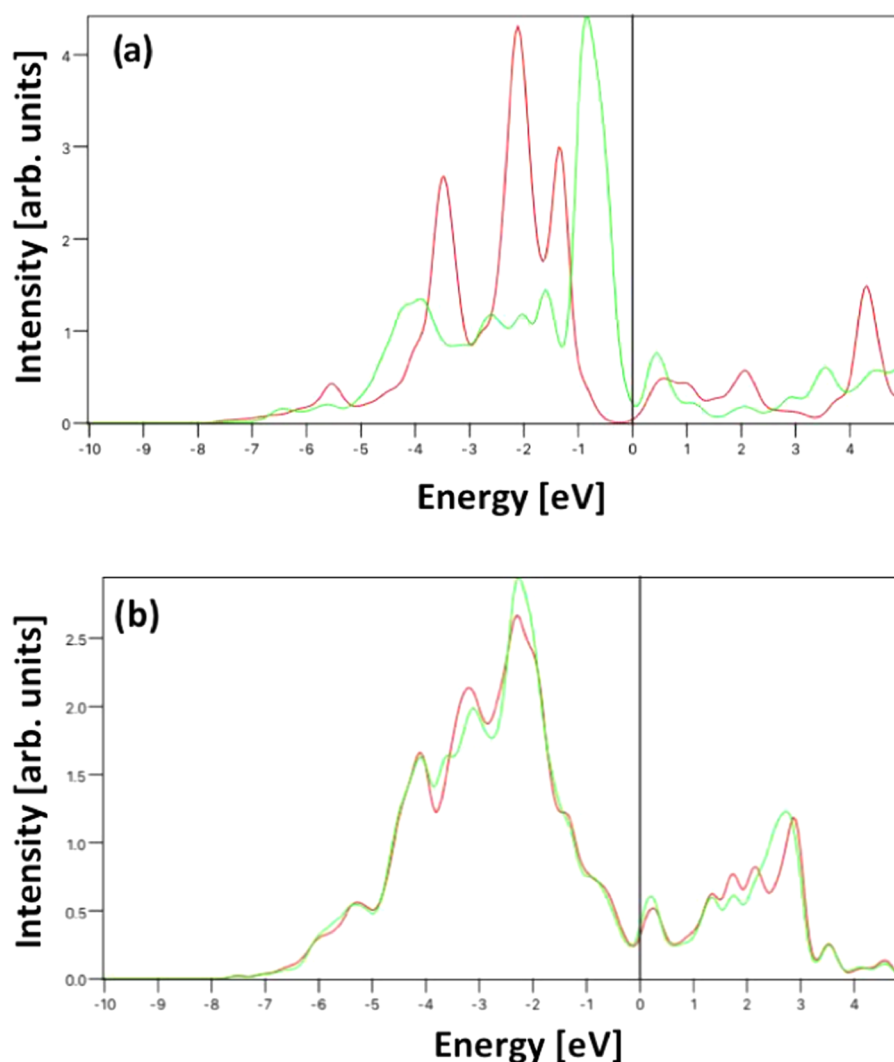
Figure 12. Projected DOS of (a) Co_9S_8 3d and (b) Co_3S_4 3d calculated by using DFT + U. Red and green lines represent stoichiometric and reduced surfaces, respectively.

Interestingly, upon sulfur vacancy formation, Co_9S_8 and Co_3S_4 show different features (see Figures 10 and 11). We calculated the site-projected pDOS for low-coordinated cobalt atoms adjacent to the sulfur vacancy and high-coordinated cobalt atoms distant from the vacancy for both surfaces. In reduced Co_3S_4, there is no significant difference between the two on site pDOS. However, reduced Co_9S_8 shows a significant difference in the intensity of the two peaks at the Fermi energy, with the 3d states of the cobalt atoms adjacent to the vacancy showing an intensity significantly higher than that by the ones distant from the vacancy, which suggests a relation with the higher catalytic activity for water dissociation in reduced Co_9S_8.

This result is in line with some hypothesis reported in the literature that suggests a relation between high HOMO occupancy at Fermi and catalytic activity.[47−49] Harris et al. correlated the t_{2g}-HOMO occupation, the TM−S bond covalence and the TM−S bond strength with the catalytic activity.[50] The more electrons in a t_{2g}-HOMO, at comparable bond strength, the better is the catalytic activity. Furthermore, Smit et al. performed DFT calculations on octahedral TM−S clusters, confirming the suggested trend between the strength of interaction between the metal 3d and the S 3p electrons and the catalytic activity.[51]

To analyze the bonding nature of Co−S, we determined the COOP by multiplying the sign of two overlapping atomic wavefunctions by the corresponding DOS, providing additional information regarding the bonding character: positive and negative values indicate bonding and antibonding interactions, respectively. Our COOP analysis suggests that for both surfaces in their stoichiometric forms, Co 3d S 3p bonding state below the Fermi energy reaches ~-2 eV. Upon vacancy formation, we notice the presence of a nonbonding state around ~-1.5 eV in Co_9S_8, whereas there is no significant change in Co_3S_4. The formation of a nonbonding state may suggest the presence of unhybridized d orbitals in reduced Co_9S_8 that enhance catalytic activity. This is also supported by the geometric features of the two surfaces that, upon vacancy formation, presents surface III and IV coordinate Co atoms in Co_9S_8 and IV and V coordinated Co atoms in Co_3S_4.

This result, being in line with the pDOS assumption of Smit et al. and Harris et al., suggests a possible enhanced catalytic activity of reduced Co_9S_8 with respect to its stoichiometric form, whereas the same trend is not predicted for Co_3S_4, confirming our conclusions presented in the previous section.
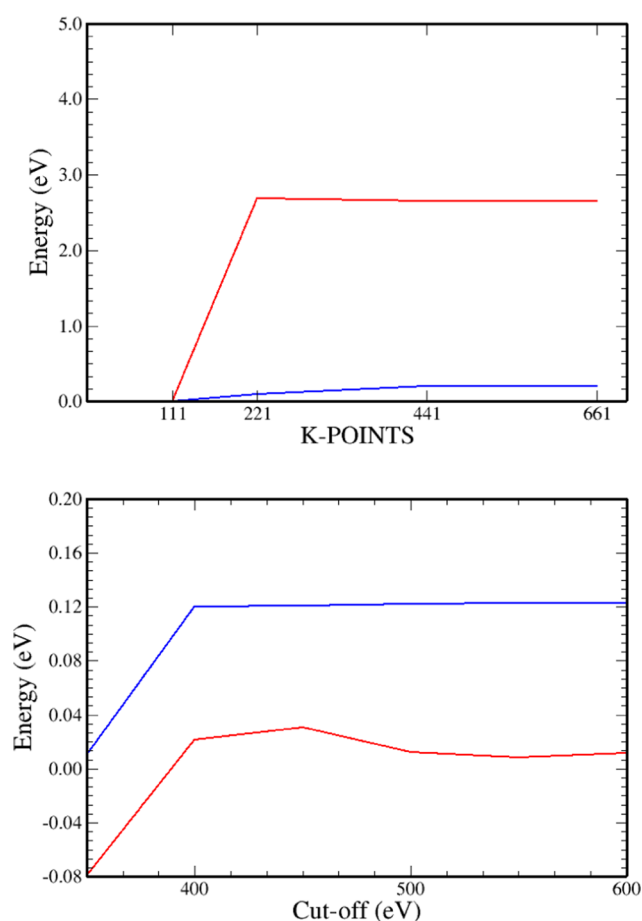
Figure 13. Change in the total energy vs increasing k-point mesh (top) and cutoff energy (bottom) for $Co_9S_8(100)$ (red line) and $Co_3S_4(100)$ (blue line).

In conclusion, the present work suggests that reduced Co_9S_8 surfaces could potentially represent suitable catalysts for water spitting and hydrogen evolution.

CONCLUSIONS

We analyzed water dissociation and hydrogen evolution reaction on $Co_9S_8(100)$ and $Co_3S_4(100)$, and we found that in Co_9S_8, sulfur vacancies play an important role in catalytic activity. On the basis of the adsorption bond strengths of the reactants, reaction intermediates, and products of water dissociation, $Co_9S_8(100)$ and $Co_3S_4(100)$ result to be particularly active for water dissociation. Furthermore, we predict that nanostructured nonstoichiometric Co_9S_8 will show an increased activity due to the low coordination of octahedral Co centers that act as active water adsorption and dissociations sites, potentially increasing the efficiency toward HER. This conclusion is supported by the electronic structure analysis. The projected density of states shows intense peaks around the Fermi energy for the low-coordinated tetragonal Co centers only in Co_9S_8. The increased water adsorption energies upon vacancy formation reflect in the increased HOMO occupancy of the low-coordinated tetrahedral Co. However, this is not seen in Co_3S_4 where vacancies do not significantly improve water adsorption and dissociation energies and do not increase the Co center DOS around the Fermi energy. The inclusion of dispersion potentials to the conventional Kohn−Sham DFT energy results in a decrease of the adsorption energies of

~15%. However, this effect is relatively larger in water, identifying the vdW character of the interaction. Our results suggest that nanostructured nonstoichiometric Co_9S_8 could in principle act as a low-temperature catalyst or co-catalyst for HER and that a test on nanoengineered surfaces is worthwhile.

APPENDIX A

In the previous section, we show the projected density of states of the two systems, comparing them. However, DFT calculations are not able to catch the d−d splitting into e_g and t_{2g} states, resulting in an overlap of degenerate 3d states. To have a correct description of the electronic structure, Hubbard correction should be introduced. However, at the moment, there is no unique choice of U that gives a satisfactory description of both the electronic structure and the energetics of the system for molecular adsorption. Also, it is not clear if the the Hubbard correction provides a systematic improvement of molecular adsorption energies if compared to DFT. Also, self-consistent methods to determine U cannot find a good agreement with experimental values.[52] As pointed out by Da Silva et al., for similar systems, there is no unique choice of U that at the same time gives a reasonable description of structural parameters, relative energies, and spectroscopic properties.[53] However, in this section, we report the projected density of states by using DFT + U (U(Co 3d) = 5 eV) to test if vacancy formation has the same effect on HOMO at the Fermi level.[54]

Figure 12 shows pDOS of stoichiometric and reduced Co_9S_8 and Co_3S_4. We obtain a d−d splitting for Co^{tetr} of ~2 eV, in line with the experimental value. Here, HOMO occupancy at Fermi is higher in reduced than stoichiometric Co_9S_8. This effect is not seen in Co_3S_4, confirming that our conclusions drawn in Electronic Structure by using by using pure GGA− DFT are adequate and correct.

APPENDIX B

We performed convergence tests for the cutoff and the k-point set, as shown in Figure 13. It can be seen that convergence to within 0.1 eV is obtained for a k-point sampling in the Brillouin zone of 2 × 2 × 1 compared with the 4 × 4 × 1 k-point set. With regard to the plane wave cutoff energy of 500 eV, employed in all our calculations, Figure 13 shows that compared with a cut−cut of 600 eV, the total energy is converged within 0.005 eV. This setup leads to an error on the adsorption energies within 0.01 eV.

AUTHOR INFORMATION

Corresponding Authors
*E-mail: marco.fronzi@mail.xjtu.edu.cn (M.F.).
*E-mail: Mike.Ford@uts.edu.au (M.J.F.).

ORCID 🔾
Marco Fronzi: 0000-0001-7855-9216

Notes
The authors declare no competing financial interest.

■ REFERENCES

(1) Kermeli, K.; Graus, W. H. J.; Worrel, E. Energy efficiency improvement potentials and a low energy demand scenario for the global industrial sector. *Energy Effic.* **2014**, *7*, 987−1011.

(2) Pleßmann, G.; Erdmann, M.; Hlusiak, M.; Breyer, C. Global energy storage demand for a 100% renewable electricity supply. *Energy Procedia* **2014**, *46*, 22−31.

(3) Walter, M. G.; Warren, E. L.; Mckone, J. R.; Boettcher, S. W.; Mi, Q.; Santor, E. A.; Lewis, N. S. Solar water splitting cells. *Chem. Rev.* **2010**, *110*, 6446−6473.

(4) Fernando, A.; Weerawardene, M.; Karimova, N. V.; Aikens, C. M. Quantum mechanical studies of large metal, metal oxide, and metal chalcogenide nanoparticles and clusters. *Chem. Rev.* **2015**, *115*, 6112.

(5) Reber, A. C.; Khanna, S. N.; Roach, P. J.; Woodward, W. H.; Castleman, A. W., Jr. Reactivity of aluminum cluster anions with water: Origins of reactivity and mechanisms for H2 release. *J. Phys. Chem. A* **2010**, *114*, 6071.

(6) Carmo, M.; Fritz, D. L.; Mergel, J.; Stolten, D. A comprehensive review on pem water electrolysis. *Int. J. Hydrogen Energy* **2013**, *38*, 4901.

(7) Bičáková, O.; Straka, P. Production of hydrogen from renewable resources and its effectiveness. *Int. J. Hydrogen Energy* **2012**, *37*, 11563.

(8) Rao, C. N. R.; Dey, S. Solar thermochemical splittig of water to generate hydrogen. *Proc. Natl. Acad. Sci. U.S.A.* **2017**, *114*, 13385−13393.

(9) Šarić, M.; Moses, P. G.; Rossmeisl, J. Relation between hydrogen evolution and hydrodesulfurization catalysis. *ChemCatChem* **2016**, *8*, 3334−3337.

(10) http://materials.springer.com/isp/crystallographic/docs/sd_0375057. Copyright 2016 Springer-Verlag Berlin Heidelberg & Material Phases Data System (MPDS), Switzerland & National Institute for Materials Science (NIMS), Japan.

(11) http://materials.springer.com/isp/crystallographic/docs/sd_0556901. Copyright 2016 Springer-Verlag Berlin Heidelberg & Material Phases Data System (MPDS), Switzerland & National Institute for Materials Science (NIMS), Japan.

(12) Sidik, R. A.; Anderson, A. B. Co9S8 as a catalyst for electroreduction of O2: quantum chemistry predictions. *J. Phys. Chem. B* **2006**, *110*, 936.

(13) Hu, H.; Han, L.; Yu, M.; Wang, Z.; Lou, X. W. Metalorganic-organic framework-engaged formation of Co nanoparticle-embedded carbon@Co9S8 double-shelled nanocages for efficient oxygen reduction. *Energy Environ. Sci.* **2016**, *9*, 107.

(14) Chang, S.-H.; Lu, M.-D.; Tung, Y.-L.; Tuan, H.-Y. Gram-scale synthesis of catalytic Co9S8 nanocrystal ink as a cathode material for spray-deposited, large-area dye-sensitized solar cells. *ACS Nano* **2013**, *7*, 9443−9451.

(15) Pan, Y.; Liu, Y.; Liu, C. Phase- and morphology-controlled synthesis of cobalt sulfide nanocrystals and comparison of their catalytic activities for hydrogen evolution. *Appl. Surf. Sci.* **2015**, *357*, 1133−1140.

(16) Sun, M.; Nelson, A. E.; Adjaye, J. Ab initio DFT study of hydrogen dissociation on MoS2, NiMoS, and CoMoS: mechanism, kinetics, and vibrational frequencies. *J. Catal.* **2005**, *233*, 411−421.

(17) Feng, L.-L.; Li, G.-D.; Liu, Y.; Wu, Y.; Chen, H.; Wang, Y.; Zou, Y.-C.; Wang, D.; Zou, X. Carbon-Armored Co9S8 Nanoparticles as All-pH Efficient and Durable H2-Evolving Electrocatalysts. *ACS Appl. Mater. Interfaces* **2015**, *7*, 980−988.

(18) Faber, M. S.; Dziedzic, R.; Lukowski, M. A.; Kaiser, N. S.; Ding, Q.; Jin, S. High-performance electrocatalysis using metallic cobalt pyrite micro- and nanostructures. *J. Am. Chem. Soc.* **2014**, *136*, 10053.

(19) Le, D.; Rawal, T. B.; Rahman, T. S. Single-layer MoS2 with sulfur vacancies: Structure and catalytic application. *J. Phys. Chem. C* **2014**, *118*, 5346−5351.

(20) Akdim, B.; Pachter, R.; Mou, S. Theoretical analysis of the combined effects of sulfur vacancies and analyte adsorption on the electronic properties of single layer MoS2. *Nanotechnology* **2016**, *27*, No. 185701.

(21) Fajín, J. L. C.; Cordeiroa, M. N. D. S.; Illas, F.; Gomes, J. R. B. Descriptors controlling the catalytic activity of metallic surfaces toward water splitting. *J. Catal.* **2010**, *276*, 92−100.

(22) Raybaud, P.; Kresse, G.; Hafner, J.; Toulhoat, H. Ab initio density functional studies of transition metal sulphides: I. crystal structure and cohesive properties. *J. Phys.: Condens. Matter* **1997**, *9*, 11085−11106.

(23) Bučko, T.; Hafner, J.; Lebègue, S.; Ángyán, J. G. Improved description of the structure of molecular and layered crystals: ab initio dft calculations with van der Waals corrections. *J. Phys. Chem. A* **2010**, *114*, 11814−11824.

(24) Perdew, J. P.; Burke, K.; Ernzerhof, M. Generalized gradient approximation made simple. *Phys. Rev. Lett.* **1996**, *77*, 3865.

(25) Kresse, G.; Furthmüller, J. Efficient iterative schemes for ab initio total-energy calculations using a plane-wave basis set. *Phys. Rev. B* **1996**, *54*, No. 11169.

(26) Kresse, G.; Furthmüller, J. Efficiency of ab-initio total energy calculations for metals and semiconductors using a plane-wave basis set. *Comput. Mater. Sci.* **1996**, *6*, 15.

(27) Kresse, G.; Hafner, J. Norm-conserving and ultrasoft pseudopotentials for first-row and transition elements. *J. Phys.: Condens. Matter* **1994**, *6*, No. 8245.

(28) Hamann, D. R.; Schlüter, M.; Chiang, C. Norm-conserving pseudopotentials. *Phys. Rev. Lett.* **1979**, *43*, No. 1494.

(29) Grimme, S.; Antony, J.; Ehrlich, S.; Krieg, S. A consistent and accurate ab initio parametrization of density functional dispersion correction (dft-d) for the 94 elements H-Pu. *J. Chem. Phys.* **2010**, *132*, No. 154104.

(30) Kresse, G.; Joubert, D. From ultrasoft pseudopotentials to the projector augmented-wave method. *Phys. Rev. B* **1999**, *59*, No. 1758.

(31) Blöchl, P. E. Projector augmented-wave method. *Phys. Rev. B* **1994**, *50*, No. 17953.

(32) Henkelman, G.; Uberuaga, B. P.; Jonsson, H. A climbing image nudged elastic band method for finding saddle points and minimum energy paths. *J. Chem. Phys.* **2000**, *113*, 9901−9904.

(33) Wyckoff, R. W. G. *Crystal Structures*; John Wiley & Sons, Academic Press: New York, 1964.

(34) Materials project, http://www.materialsproject.org

(35) Jain, A.; Ong, S. P.; Hautier, G.; Chen, W.; Richards, W. D.; Dacek, S.; Cholia, S.; Gunter, D.; Skinner, D.; Ceder, G.; Persson, K. A. The Materials Project: A materials genome approach to accelerating materials innovation. *APL Mater.* **2013**, *1*, No. 011002.

(36) FIZ Karlsruhe. Inorganic Crystal Structure Database.

(37) Heyrovský, J. A theory of overpotential. *Recl. Trav. Chim. Pays-Bas* **1927**, *46*, 582.

(38) Erdey-Gruz, T.; Volmer, M. Zur theorie der wasserstoff Überspannung. *Z. Phys. Chem. A* **1930**, *150A*, 203−213.

(39) Tafel, J. Über die polarisation bei kathodischer wasserstoffent-wicklung. *Z. Phys. Chem.* **1905**, *50U*, 641−712.

(40) Kostov, M. K.; Santiso, E. E.; George, A. M.; Gubbins, K. E.; Buongiorno Nardelli, M. Dissociation of water on defective carbon substrates. *Phys. Rev. Lett.* **2005**, *95*, No. 136105.

(41) Muhich, C. L.; Ehrhart, B. D.; Witte, V. A.; Miller, S. L.; Coker, E. N.; Musgrave, C. B.; Weimer, A. W. Predicting the solar thermochemical water splitting ability and reaction mechanism of metal oxides: a case study of the hercynite family of water splitting cycles. *Energy Environ. Sci.* **2015**, *8*, 3687.

(42) Nørskov, J. K.; Bligaard, T.; Logadottir, A.; Kitchin, J. R.; Chen, J. G.; Pandelov, S.; Stimming, U. Trends in the exchange current for hydrogen evolution. *J. Electrochem. Soc.* **2005**, *152*, J23−J26.

(43) Rossmeisl, J.; Logadottir, A.; Nørskov, J. K. Electrolysis of water on (oxidized) metal surfaces. *Chem. Phys.* **2005**, *319*, 178−184.

(44) Fronzi, M.; Piccinin, S.; Delley, B.; Traversa, E.; Stampfl, C. Water adsorption on the stoichiometric and reduced CeO2(111) surface: a first-principles investigation. *Phys. Chem. Chem. Phys.* **2009**, *11*, 9188−9199.

(45) Fronzi, M.; Piccinin, S.; Delley, B.; Traversa, E.; Stampfl, C. CHx adsorption (x = 1−4) and thermodynamic stability on the CeO2(111) surface: a first-principles investigation. *RSC Adv.* **2014**, *4*, 12245−12251.

(46) Jackson, A. J.; Tianaa, D.; Walsh, A. A universal chemical potential for sulfur vapours. *Chem. Sci.* **2016**, *7*, 1082−1092.

(47) Aray, Y.; Rodriguez, J.; Vega, D.; Rodriguez-Arias, E. N. Correlation of the topology of the electron density of pyrite type transition metal sulfides with their catalytic activity in hydro-desulfurization. *Angew. Chem., Int. Ed.* **2000**, *39*, 3810.

(48) Zonnevylle, M. C.; Hoffmann, R.; Harris, S. Thiophene hydrodesulfurization on MoS2; theoretical aspects. *Surf. Sci.* **1988**, *199*, 320.

(49) Rodriguez, J. A. Interaction of hydrogen and thiophene with Ni/MoS2 and Zn/MoS2 surfaces: a molecular orbital study. *J. Phys. Chem. B* **1997**, *101*, 7524.

(50) Harris, S.; Chianelli, R. R. Catalysis by transition metal sulfides: The relation between calculated electronic trends and hds activity. *J. Catal.* **1984**, *86*, 400.

(51) Smit, T. S.; Johnson, K. H. A unified theory of periodic and promotion effects in transition metal sulphide hydrodesulphurization catalysts. *Catal. Lett.* **1994**, *28*, 361.

(52) Shishkin, M.; Sato, H. Self-consistent parametrization of dft + u framework using linear response approach: Application to evaluation of redox potentials of battery cathodes. *Phys. Rev. B* **2016**, *93*, No. 085135.

(53) Da Silva, J. L. F.; Ganduglia-Pirovano, M. V.; Sauer, J.; Baye, V.; Kresse, G. Hybrid functionals applied to rare-earth oxides: The example of ceria. *Phys. Rev. B* **2007**, *75*, No. 045121.

(54) Assadi, M. H. N.; Katayama-Yoshida, H. Dopant incorporation site in sodium cobaltate's host lattice: a critical factor for thermoelectric performance. *J. Phys.: Condens. Matter* **2015**, *27*, No. 175504.